

The nested morphology of disk winds from young stars revealed by JWST/NIRSpec observations

Received: 27 February 2024

Accepted: 10 September 2024

Published online: 04 October 2024

 Check for updates

Ilaria Pascucci¹✉, Tracy L. Beck², Sylvie Cabrit^{3,4}, Naman S. Bajaj¹, Suzan Edwards⁵, Fabien Louvet⁴, Joan R. Najita⁶, Bennett N. Skinner^{1,7}, Uma Gorti^{8,9}, Colette Salyk¹⁰, Sean D. Brittain¹¹, Sebastiaan Krijt¹², James Muzerolle Page¹², Maxime Ruaud⁸, Kamber Schwarz¹³, Dmitry Semenov^{13,14}, Gaspard Duchêne^{4,15} & Marion Villenave¹⁶

Radially extended disk winds could be the key to unlocking how protoplanetary disks accrete and how planets form and migrate. A distinctive characteristic is their nested morphology of velocity and chemistry. Here we report James Webb Space Telescope near-infrared spectrograph spectro-imaging of four young stars with edge-on disks, three of which have already dispersed their natal envelopes. For each source, a fast collimated jet traced by [Fe II] is nested inside a hollow cavity within wider lower-velocity H₂. In one case, a hollow structure is also seen in CO ro-vibrational ($\nu = 1 \rightarrow 0$) emission but with a wider opening angle than the H₂, and both of those are nested inside an Atacama Large Millimeter Array CO ($J = 2 \rightarrow 1$) cone with an even wider opening angle. This nested morphology, even for sources with no envelope, strongly supports theoretical predictions for wind-driven accretion and underscores the need for theoretical work to assess the role of winds in the formation and evolution of planetary systems.

The assembly of stars and their planetary systems proceeds through an accretion disk, in which magneto-rotational instability¹ was long favoured for transporting angular momentum outward to aid inward accretion. Recent simulations incorporating disk microphysics challenge this view and show that magneto-rotational instability is suppressed in most of the planet-forming region (~1–20 au). Instead, radially extended magnetohydrodynamic (MHD) disk winds—outflowing gas from a few scale heights above the disk midplane launched by magnetic and thermal pressures—emerge as a viable mechanism for

angular momentum removal and for enabling accretion (ref. 2 and references therein). This new wind-driven accretion scenario greatly impacts the evolution of the disk surface density³, thus affecting the inward drift of solids⁴ and where planets may form and migrate to⁵. Consequently, observations that can confirm the presence of these winds are crucial.

A unique feature of radially extended MHD winds is that flows are launched over a broad range of disk radii, hence outflow velocities, from near the gas co-rotation radius (~0.1 au) and across much

¹Lunar and Planetary Laboratory, The University of Arizona, Tucson, AZ, USA. ²Instruments Division, Space Telescope Science Institute, Baltimore, MD, USA. ³Observatoire de Paris - PSL University, Sorbonne Université, LERMA, CNRS, Paris, France. ⁴Univ. Grenoble Alpes, CNRS, IPAG, Grenoble, France.

⁵Five College Astronomy Department, Smith College, Northampton, MA, USA. ⁶NSF, NOIRLab, Tucson, AZ, USA. ⁷Department of Physics and Astronomy, McMaster University, Hamilton, Ontario, Canada. ⁸Carl Sagan Center, SETI Institute, Mountain View, CA, USA. ⁹Ames Research Center, NASA, Moffett Field, CA, USA. ¹⁰Department of Physics and Astronomy, Vassar College, Poughkeepsie, NY, USA. ¹¹Department of Physics and Astronomy, Clemson University, Clemson, SC, USA. ¹²Department of Physics and Astronomy, University of Exeter, Exeter, UK. ¹³Max-Planck-Institut für Astronomie, Heidelberg, Germany. ¹⁴Department of Chemistry, Ludwig-Maximilians-Universität, Munich, Germany. ¹⁵Department of Astronomy, University of California, Berkeley, CA, USA. ¹⁶Dipartimento di Fisica, Università degli Studi di Milano, Milan, Italy. ✉e-mail: pascucci@arizona.edu

Table 1 | Source properties from the literature relevant to this study

Source	Right ascension (J2000)	Declination (J2000)	M_*	F_{mm}	PA_{mm}	i_{mm}	R_{mm}	R_{ir}	Refs.
	(hmins)		(M_{\odot})	(mJy)	($^{\circ}$)	($^{\circ}$)	(au)	(au)	
FS Tau B	42200.7	+26°57'32.5"	0.7	341	145	74	144	161	21,59
HH 30	43137.5	+18°12'24.5"	0.5	55	121	>85	130	217	21,38
IRAS 04302	43316.5	+22°53'20.4"	1.3–1.7	268	175	>84	220		21,59
Tau 042021	42021.4	+28°13'49.2"	0.4	124	–16	>85	287	350	21,60

M_* was inferred from the Keplerian rotation of the disk gas, observed through well-resolved millimetric-wavelength spectro-imaging of molecular lines. F_{mm} , PA_{mm} , i_{mm} and R_{mm} are the flux density, position angle, inclination and disk radius from spatially resolved ALMA band 7 (0.89 mm) continuum images, which trace millimetre-sized grains. R_{ir} is the disk radius from optical/near-infrared scattered light images, thus probing small submicrometre grains coupled well with the gas.

of the planet-forming region (for example, ref. 6). This contrasts with X-winds, in which stellar field lines couple narrowly to the disk at the co-rotation radius and launch fast MHD winds ($\sim 150 \text{ km s}^{-1}$) that spread widely⁷ and photoevaporative winds, which develop only where the disk gas has enough thermal energy to escape the stellar gravitational field, namely beyond $\sim 1 \text{ au}$ and with speeds $\leq 10 \text{ km s}^{-1}$ (ref. 8). Another distinctive characteristic of radially extended MHD winds is their nested morphology of velocity and chemistry throughout all stages of star-disk evolution. A fast $\sim 100 \text{ km s}^{-1}$ jet, formed by the recollimation of the inner wind, lies inside atomic and molecular gas moving at sequentially lower velocities (for example, ref. 9). X-winds can also collimate a jet (for example, ref. 10). However, lower-velocity flows arise solely from material entrained by the fast wind, which sweeps up gas near the disk surface¹¹ and, when an infalling envelope is present, also gathers envelope material near the disk's outer edge¹². Conversely, in the photoevaporative scenario, the absence of recollimation means fast jets are not produced and the wind's opening angle remains close to that at launch (for example, ref. 13).

Current kinematic data on young stars (~ 0.1 – 10 Myr) with a mass greater than that of the infalling envelope—class I and II sources¹⁴—hint at the presence of radially extended MHD winds. Spatially unresolved spectra of optical forbidden emission, like [O I] and near-infrared emission of H_2 , can show, in addition to a high-velocity component (~ 50 – 300 km s^{-1}) tracing the base of a jet, a second lower-velocity component with broad linewidths, which is interpreted as originating over disk radii ~ 0.5 – 5 au (for example, ref. 15). A handful of spatially resolved outflows point to velocities that decrease outwards, with the narrow fast jet along the axis of a wider-angle lower-velocity flow (ref. 16 and references therein). However, the limited number of spatially resolved flows, especially for sources that have dispersed their natal envelopes (for example, refs. 17–19), has thus far hindered a detailed mapping of the wind morphology across chemical species, leaving the predicted nested structure by radially extended MHD winds uncertain.

Results

We used the near-infrared spectrograph (NIRSpec) on the James Webb Space Telescope (JWST)²⁰ to acquire deep spectro-imaging of four edge-on disks with known jets (for example, ref. 21). All sources belong to the nearby ($\sim 140 \text{ pc}$) and young (~ 1 – 2 Myr) Taurus star-forming region (for example, ref. 22). See Table 1 for their properties relevant to this study. Although infrared spectral indices are often used to assign classes to young stellar systems as proxies for their evolutionary stage (for example, ref. 23), this method is unreliable for edge-on disks²⁴. Comparing the millimetre disk fluxes recorded by the Atacama Large Millimeter Array (ALMA; Table 1) with single-dish fluxes^{25–28} revealed that only IRAS 04302 is surrounded by an envelope. The other sources' fluxes are primarily from disk emission, which suggests that they are at a more evolved evolutionary stage with no notable infalling envelope that aligns with the class II category.

The integral field unit (IFU) of NIRSpec covers a field of view of $\sim 3'' \times 3''$ with a pixel scale of $0.1''$ and, with our use of the three high-resolution gratings, delivers 0.95 – $5.27 \mu\text{m}$ spectra at each pixel with a velocity sampling of $\sim 40 \text{ km s}^{-1}$ (see Methods for details on the observations and data reduction). Several [Fe II], H and H_2 lines were detected in the integrated spectra along with the P- and R-branches of the CO ($v=1 \rightarrow 0$) ro-vibrational transition at $\sim 4.7 \mu\text{m}$ (some of the detected lines are highlighted in Fig. 1). We focused on the brightest [Fe II] line at $1.644 \mu\text{m}$, a known jet tracer (for example, ref. 29), the H_2 $0 \rightarrow 0 \text{ S}(9)$ line at $4.695 \mu\text{m}$, and the CO ($v=1 \rightarrow 0$) band. We selected the H_2 S(9) line, the brightest long-wavelength transition in our sample, due to its considerably lower scattering from the disk surface relative to shorter-wavelength H_2 lines, like the often-studied $2.12 \mu\text{m } 1 \rightarrow 0 \text{ S}(1)$ line. Its integrated flux is at most half that of the S(1) line (Table 2 and Methods). Thus, it combines the advantages of tracing the H_2 morphology closer to the disk with considerable relative brightness. The similarity of the [Fe II] fluxes in our sample (Table 2) hints at similar jet mass-loss rates. Considering the estimate for HH 30 of $2 \times 10^{-9} M_{\odot} \text{ yr}^{-1}$ (ref. 30) and factoring in the typical jet/accretion ratio of approximately 0.1 (ref. 31), it is probable that our sources are accreting at rates exceeding $10^{-8} M_{\odot} \text{ yr}^{-1}$. This inference is supported by the sole mass accretion rate available in the literature for our sample, that for FS Tau B, which is $\sim 1.5 \times 10^{-7} M_{\odot} \text{ yr}^{-1}$ (ref. 32).

Figure 2 shows continuum-subtracted line maps after the point spread function (PSF) deconvolution of the $1.644 \mu\text{m}$ [Fe II] line, the H_2 $0 \rightarrow 0 \text{ S}(9)$ line, along with the sum of the CO P-branch lines between ~ 4.7 and $4.9 \mu\text{m}$ (see Methods for details). The continuum emission below the H_2 S(9) line, which traces light scattered by small grains at the disk surface, is also displayed in one panel in each row. The main panels show three-colour composite images combining the [Fe II] and H_2 lines with the continuum emission. Additionally, integrated CO P-branch contours are overlaid in grey. [Fe II] traces the narrow jet emission, and we verified that its position angle (PA) was perpendicular to the ALMA millimetre disk (Tables 1 and 2). We also generated H_2 maps for the $1 \rightarrow 0 \text{ S}(1)$ at $2.12 \mu\text{m}$ and the $0 \rightarrow 0 \text{ S}(8)$ at $5.05 \mu\text{m}$ lines and found similar morphologies to the H_2 $0 \rightarrow 0 \text{ S}(9)$ line, which is, thus, representative for the molecular hydrogen gas. In addition, we created velocity centroid maps for the [Fe II] and H_2 lines and found that the NIRSpec resolution can discern small shifts between the blue lobe and red lobe of the [Fe II] jets (Methods). The images in Fig. 2 have been rotated to align the blueshifted jet emission vertically at the top of each panel. The H_2 maps show no resolved velocity structure, as expected if the molecular gas is moving more slowly than the jet.

For each source, the narrow [Fe II] jet is nested within wider H_2 emission, which is always more vertically extended than the continuum emission at the same wavelength. Although the overall [Fe II]/ H_2 morphology, with a narrow atomic jet along the axis of a wider H_2 cone, has been seen in a few other sources (for example, refs. 17,33,34), we identify the presence of a central cavity in the H_2 cone. Emission in a cone with a hollow centre, in the absence of ambient material, is expected if

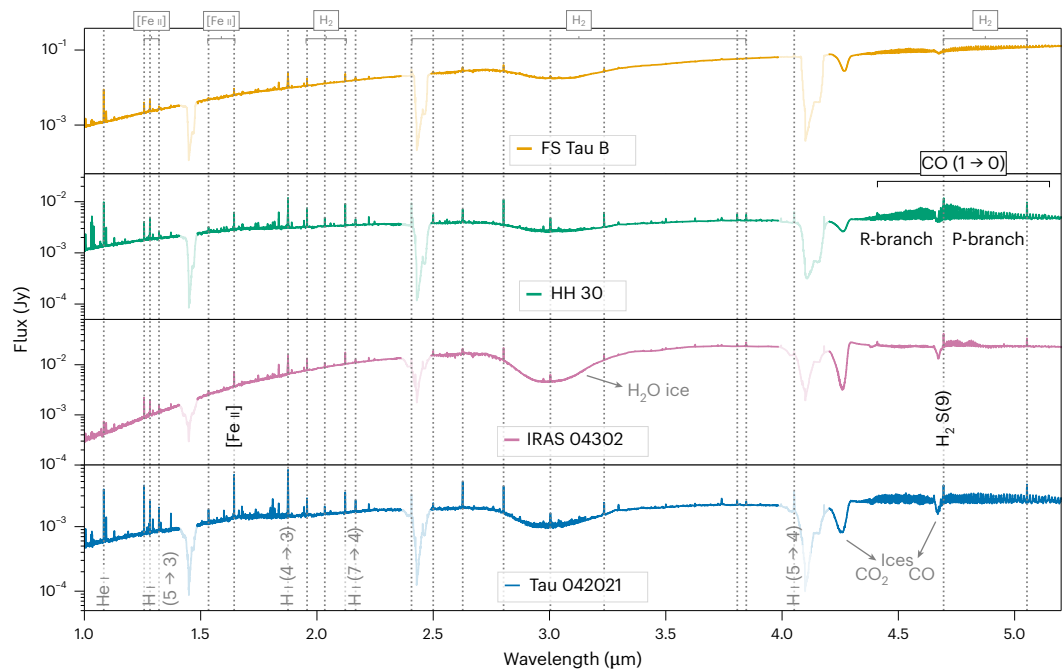


Fig. 1 | Spectra integrated over the NIRSpec IFU. Semitransparent regions indicate the minimum and maximum wavelength cutoffs of the detectors' gaps. The H₂O, CO₂ and CO ice bands are identified with grey arrows. A few of the strongest emission lines are marked with grey dotted lines. All these lines are spatially extended. The transitions analysed in this study are highlighted in bold.

Table 2 | Inferred jet and wind properties

Source	Jet: [Fe II] 1.644 μm			Wind: H ₂ O → O S(9) 4.695 μm		
	Flux (ergs ⁻¹ cm ⁻²)	PA (°)	θ _j (°)	Flux (ergs ⁻¹ cm ⁻²)	θ _w (°)	R _{geo} (")
FS Tau B	4.1×10 ⁻¹⁵	55±3	16.8±2.5	3.5×10 ⁻¹⁵	41.2±7.9	-0.05±0.15
					50.3±2.3	-0.03±0.05
HH 30	2.0×10 ⁻¹⁵	32±2	2.6±0.5	1.5×10 ⁻¹⁵	14.1±0.5	-0.04±0.01
					12.8±0.5	0.05±0.01
IRAS 04302	3.0×10 ⁻¹⁵	87±2	7.5±0.9	4.0×10 ⁻¹⁵	38.7±3.8	-0.04±0.09
					27.8±1.8	0.04±0.03
Tau 042021	3.2×10 ⁻¹⁵	72±2	5.3±1.0	4.5×10 ⁻¹⁶	38.5±4.5	-0.02±0.08
					37.6±2.6	0.04±0.05

The [Fe II] and H₂ lines we have selected are among the most prominent tracers of jets and winds, respectively. For each source, we list the jet's semi-opening angle (θ_j) and the wind's semi-opening angle (θ_w) and extrapolated radius at z=0 (R_{geo}) for both lobes of the blueshifted emission. The quoted uncertainties on these values are one standard deviation. FS Tau B's disk is less inclined than the others. Hence, the disk plane and R_{geo} are less well determined (Methods). The uncertainty in the integrated line fluxes is dominated by the 10% absolute photometric accuracy of the NIRSpec spectra (Methods)³⁰.

H₂ traces material lifted from the disk, that is a disk wind that emerges at a larger radial distance than the jet (for example, ref. 9). Extended CO ro-vibrational emission is detected for three of the sources. Uniquely for HH 30, this emission mirrors the H₂ conical morphology, albeit less vertically extended, with a central cavity surrounding the jet. This represents the resolved mapping of a wind-like structure in the CO (ν = 1 → 0) band (see ref. 35 and references therein for hints of winds in this tracer through spectro-astrometry).

A notable brightness asymmetry relative to the disk plane is seen in the jet and wind features for two of our sources, FS Tau B and HH 30. In both cases, the more prominent emission is on the side of the disk where the jet is blueshifted. Although this asymmetry was already known for their jets^{36,37}, it has now been seen in the winds as well. This discovery is particularly noteworthy for FS Tau B, marking the first such observation in its wind. For HH 30, our finding corroborates the asymmetry previously noted in the millimetre CO (J = 2 → 1) wind emission³⁸.

For each source, we traced the [Fe II] jet and H₂ wind emission to quantify their semi-opening angles (θ_j and θ_w) and estimate the radii where the wind intersects the disk plane (geometric radii, R_{geo}). See Methods for details and Table 2 for the results. The jet semi-opening angles vary between -2.5° and -17°, consistently smaller than their corresponding wind semi-opening angles, which range from -13° to 50°. HH 30 stands out as having the most collimated jet and the narrowest wind among our sources (Fig. 3), although similarly narrow jets have been reported in other class II sources (for example, ref. 39). The wind semi-opening angle that we estimate for Tau 042021 is the same as that recently reported in ref. 19 using a lower spatial resolution H₂ S(2) map obtained with the mid-infrared instrument (MIRI) onboard JWST. Our PSF-deconvolved images enable us to measure the semi-opening angle of its jet, which was unresolved with MIRI. In addition, we can place stringent constraints on the intersection points of the H₂ cones with the disk plane. Specifically, we determine that these intersections

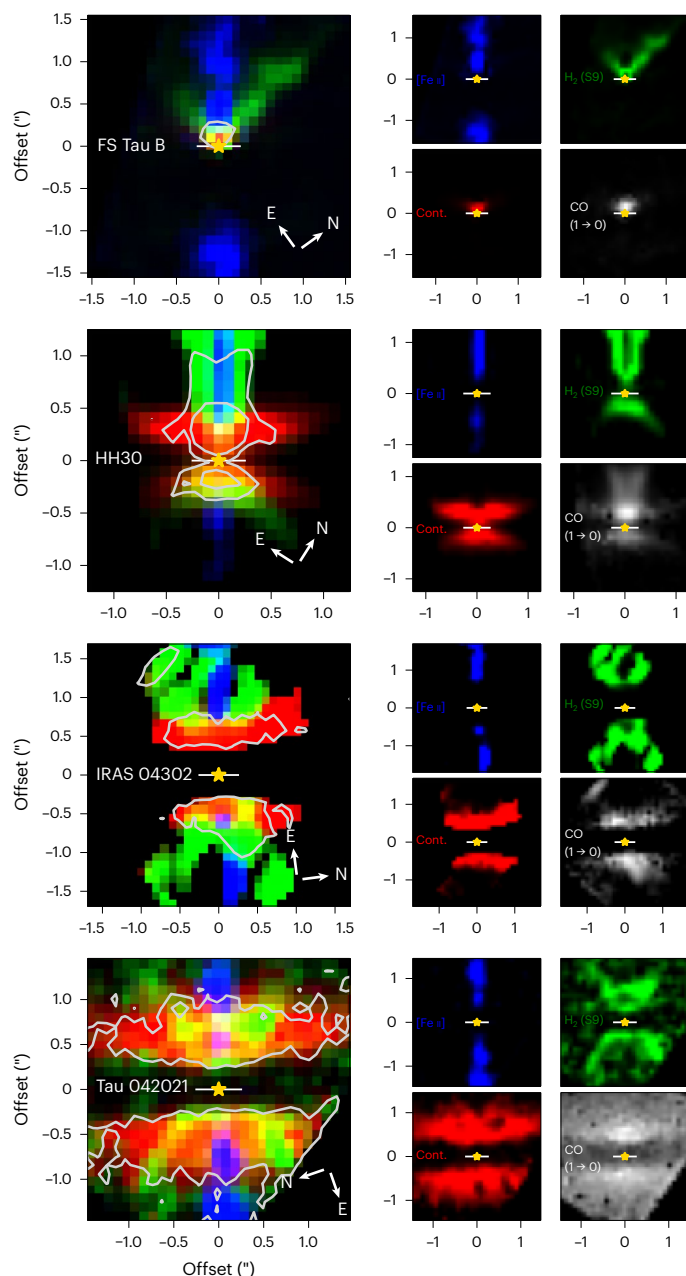


Fig. 2 | Composite NIRSpec images. [Fe II] emission at 1.644 μm in blue, H_2 $\text{S}(9)$ emission at 4.695 μm in green and the continuum emission (Cont.) at the H_2 line in red. CO emission from $\sim 4.7\text{--}4.9$ μm is shown in the right bottom panels of each row in grey. The 50% of the peak emission contour (and for HH 30 also the 30%) is shown in grey in each composite image. In every instance, the collimated jet traced by [Fe II] is nested inside the wider H_2 emission and, for HH 30, also the CO ($\nu=1 \rightarrow 0$) emission.

occur at $R_{\text{geo}} < 0.1''$ (Table 2; 14 au at the average distance of Taurus), well inside the disk outer radii of $\sim 150\text{--}350$ au. If these cones trace MHD winds, the decreasing wind opening angle with height due to magnetic recollimation (for example, ref. 40) implies that each R_{geo} defines an upper boundary for the actual wind-launching radius.

Discussion and conclusions

Different types of disk winds, with distinct kinematic and morphological features, have been discussed in the literature review. X-winds have been invoked to spin down the accreting star⁷, whereas photoevaporative winds might drive disk dispersal⁸. Only radially extended MHD

winds could solve the long-standing puzzle of how protoplanetary disks accrete (see refs. 2,16, for recent reviews).

The edge-on orientations of our systems provide a unique advantage when mapping out the structure of their disk winds, as the bright flux of the central star is effectively masked by the disk. The NIRSpec IFU spectral imaging has revealed the morphology of the atomic and molecular disk wind components in striking detail for several class II systems, on spatial scales reaching down to 30 au from the disk plane. In all cases, a collimated jet traced by [Fe II] is encased within the wider-angle emission from H_2 , and in one case, also CO ($\nu=1 \rightarrow 0$). The near-infrared molecular emission extends well above 100 au from the disk plane with a characteristic conical shape previously noted in a few other systems (for example, refs. 17–19). The consistent detection of a pronounced central cavity, marked by a notable absence of emission at the H_2 axial position, is an important finding. Moreover, the molecular wind emission appears to be anchored at radial distances < 15 au, well inside the disk radii. High-resolution ground-based spectroscopy of class I and II sources has found low-velocity H_2 2.12 μm flows reaching blueshifted speeds of up to ~ 20 km s^{-1} (for example, ref. 15). Although H_2 velocities were not measured for our edge-on sources ('Results'), similarly low velocities probably characterize the molecular structures that we have imaged.

For HH 30, we also compared the brightest component of the wind traced with NIRSpec in H_2 and CO ($\nu=1 \rightarrow 0$) with that probed with ALMA in the CO ($J=2 \rightarrow 1$) line, as shown in the left panel of Fig. 4. The CO millimetre emission traces gas flowing at ~ 10 km s^{-1} and has a hollow cone shape but with a semi-opening angle of $\sim 35^\circ$ (ref. 38), considerably wider than the $\sim 13^\circ$ and $\sim 18^\circ$ semi-opening angles of the warmer H_2 and CO ($\nu=1 \rightarrow 0$) cones (Table 2 and caption of Fig. 4). The latter nestle inside the millimetre cavity and, as expected, the average R_{geo} derived from H_2 ($\sim 6 \pm 2$ au) falls below the ~ 10 au deduced from the CO ($J=2 \rightarrow 1$) emission³⁸. These distinctive nested hollow structures might be less discernible at lower disk inclinations. However, observations at lower inclinations provide complementary information, especially for the flow velocity, when performed with high-resolution spectroscopy.

Three of our systems appear to have dispersed most of their primordial envelopes ('Results'), as indicated by the similarity of the single-dish continuum millimetre fluxes and the ALMA disk fluxes. The absence of an envelope disfavors scenarios in which the observed wide-angle lower-velocity molecular flows trace infalling envelope material swept up and entrained by an X-wind or the jet itself^{41,42}. Additionally, our R_{geo} values are more than an order of magnitude smaller than the disk radii, which are the base of the X-wind swept-up shell⁴³. The alternative of lower-velocity material entrained at the disk surface by a wide-angle X-wind¹¹ can also be excluded given the vertical extent and semi-opening angle $\leq 50^\circ$ of the H_2 emission detected with NIRSpec. Thus, although jet production by the X-wind cannot be ruled out, its role in generating the observed molecular flows seems very unlikely.

Photoevaporative winds produce molecular flows only beyond several astronomical units and with velocities of just a few km s^{-1} and opening angles of around 45° (for example, ref. 44). Photoevaporative winds struggle to account for H_2 flows exceeding 5 km s^{-1} and cannot match the 100 au vertical extent seen in our NIRSpec data (see ref. 45 for the predicted H_2 2.12 μm -emitting region). Moreover, the near-infrared H_2 and CO cones observed in HH 30 are narrower (Fig. 4) than those predicted by photoevaporative winds, and the mass flux derived from CO ALMA data exceeds typical photoevaporative mass-loss rates^{13,38,45}. Importantly, photoevaporative winds do not recollimate to produce fast axial jets. Hence, they would need to be coupled with an MHD wind to reproduce the narrow [Fe II] emission seen in our sample. These inner winds might shield high-energy photons from the central star, diminishing their capacity to reach the outer disk and drive photoevaporative flows (Fig. 8 in ref. 16). The absence of [Ne II] 12.8 μm low-velocity flows from stars with accretion rates $\geq 10^{-8} M_\odot \text{yr}^{-1}$, akin to those of our

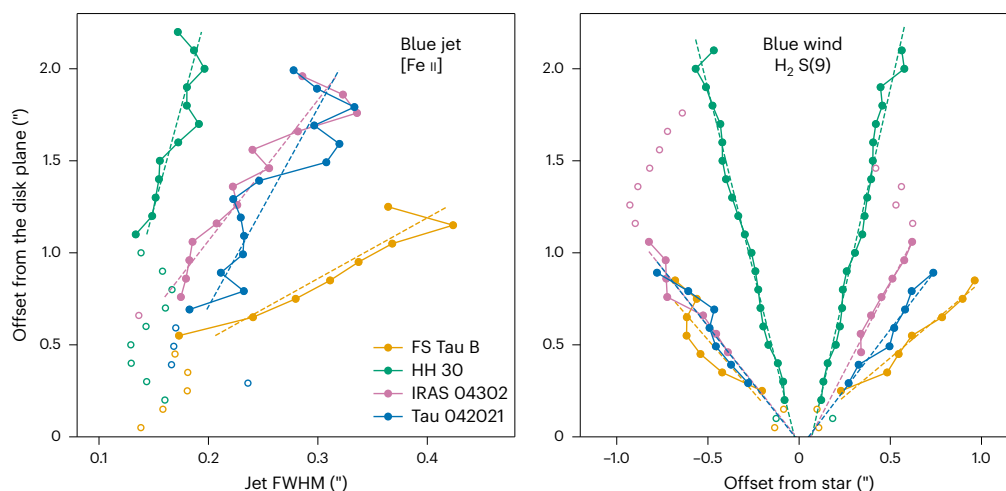


Fig. 3 | Traces of the outer edges of the [Fe II] at 1.644 μm and $\text{H}_2\text{S}(9)$ emission. Left, FWHM of the jet's blueshifted component as a function of distance from the disk plane. Right, edges of the wind's blueshifted component versus the disk's plane. In both panels, filled symbols represent data points used in the linear fit to estimate the jet and the wind semi-opening angles and R_{geo}

(Table 2). The best fits are shown with dashed lines. Data points near the disk plane are not included in the fit due to inadequate sampling of the FWHM and scattering (see Methods for details). For IRAS 04302, we excluded points above 1.2" as they clearly deviate from a wind-like morphology. HH 30 has the narrowest jet and wind in our sample.

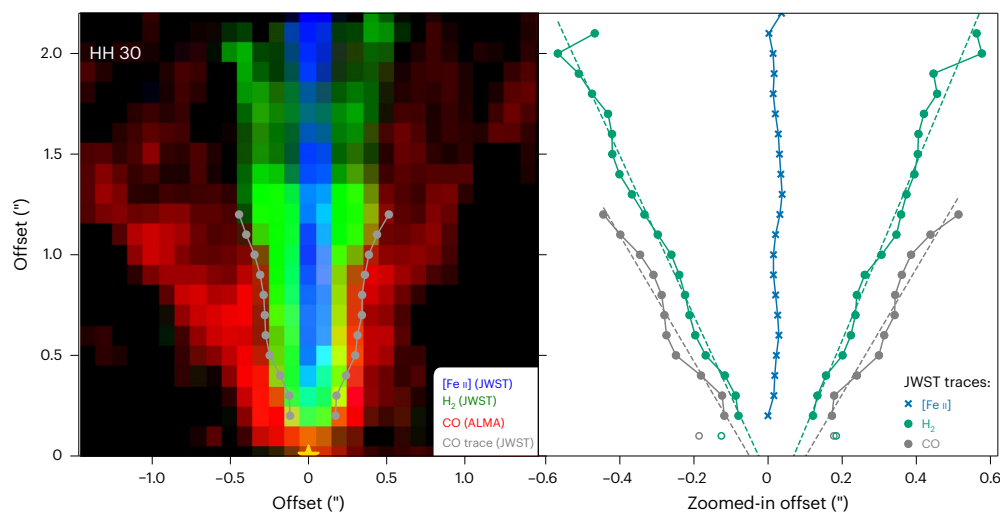


Fig. 4 | Emission structures of [Fe II], H_2 and CO in HH 30. Left, composite image of [Fe II] at 1.644 μm (blue), H_2 at 4.695 μm (green), ALMA CO (2 \rightarrow 1) in the local standard of rest velocity $8.3 \pm 0.3 \text{ km s}^{-1}$ (red) and after removing the disk emission³⁸. The NIRSpect CO ($\nu = 1 \rightarrow 0$) traces of the outer edges are shown in grey. Right, trace of the [Fe II] jet centroid (blue) and traces of the outer edges of the H_2 (green) and CO ($\nu = 1 \rightarrow 0$, grey) components detected with NIRSpect.

The CO ($\nu = 1 \rightarrow 0$) semi-opening angle and geometric radius are $17.8^\circ \pm 2.5^\circ$ and $0.075'' \pm 0.025''$ ($10.5 \pm 3.5 \text{ au}$), respectively. These are larger than those measured in H_2 ($13.5^\circ \pm 1.1^\circ$ and $0.045'' \pm 0.01''$; see also Table 2). With the NIRSpect H_2 outer edge inside that of the CO ($\nu = 1 \rightarrow 0$) and both emissions enclosed within the cooler ALMA CO wind, this figure demonstrates the nested structure of disk winds.

sources ('Results'), coupled with low-velocity [O I] tracing an inner wind, strongly suggests such shielding (see Section 4.2 in ref. 16).

Among the proposed wind models, radially extended MHD winds are the only ones that are consistent with the wind morphologies and nested structures observed in our sample. Although the initial opening angles at the launch radii are $\geq 30^\circ$, the toroidal component of the magnetic field produces a gradual recollimation (for example, ref. 40). Field lines close to the co-rotation radius contribute to a fast axial jet, whereas those further out can explain a range of flow opening angles depending on the scale probed by the observations. With the temperature, ionization and radiation field decreasing as the launch radius increases, a nested velocity structure and morphology are expected (for example, ref. 6). H_2 and CO can survive in these winds and trace photoprocesses like those in photodissociation regions and internal shocks⁹. The one-sided winds of FS Tau B and HH 30 are aligned with

global MHD simulations that account for the non-ideal Hall effect⁴⁶, although differences in the ambient medium, more pronounced in embedded sources, might also contribute to the asymmetry (for example, ref. 34).

The rich spectral information in this NIRSpect dataset, with numerous lines of [Fe II], H_2 , and CO (Fig. 1), enables the physical conditions in the wind components to be determined, including mass-loss rates (N.S.B. et al., manuscript in preparation, and T.L.B. et al., manuscript in preparation). Together, the imaging and spectroscopy will clarify whether disk winds are, indeed, sufficient to drive disk accretion. The implications of wind-driven accretion extend far beyond clarifying how disks accrete. Wind-driven accretion profoundly impacts disk dynamics and planet formation: it slows down the inward drift of solids, thus helping to overcome the radial drift barrier that hinders planet formation⁴, and it alters the migration of planetary embryos, which

enhances the survival of close-in super-Earths⁵. Additionally, MHD winds could transport high-temperature materials from the inner Solar System to the comet-forming region⁴⁷. These effects could reshape our understanding of how planetary systems form and evolve.

Methods

Observations and data reduction

Our sources were observed in September 2022 with the JWST NIRSpec IFU instrument as part of our cycle 1 general observer programme (PI Pascucci, ID 1621). We adopted a four-point dither pattern to improve the sampling of the PSF, one integration with 30 groups per dither and integrated for a total on-source time of 30 min per grating. We selected all three high-resolution gratings to cover the entire wavelength range from -0.98 to $5.2\ \mu\text{m}$.

To reduce the data, we used the JWST calibration pipeline⁴⁸ v.1.13.4.dev19+gbddb39c6, which was made available on 25 January 2024. The initial stage, Detector1Pipeline, implements detector-level corrections on a group-by-group basis. We customized the jump step within this stage to detect ‘snowballs’ in the data and flagged groups after the jump with a data number above 1,000 and any groups within the first 50 s. Subsequently, the Spec2Pipeline was executed with default parameters and NSClean on; this step includes photometric calibration, flat field correction and World Coordinate System assignment. Because of issues with the default outlier detection and rejection step within the Spec3Pipeline stage, we ran a custom script to flag very large positive and negative pixels (J. Morrison, personal communication, 2023). Following this, we ran the Spec3Pipeline with the modified cal files and created the image cubes with and without the ifualign mode. The latter avoids any further interpolation and is the preferred product for the analysis carried out in this paper. We inspected the cubes to verify that none of the scientific data were erroneously flagged.

Finally, to properly compare NIRSpec IFU data across the full wavelength range in the dataset, the measured data cubes were deconvolved at each wavelength using a corresponding model PSF. How the deconvolution model PSF is derived is described in the next paragraph. Deconvolution was carried out using the robust Bayesian-based Richardson–Lucy method^{49,50}, which conserves flux. Iterations were optimized and visually inspected to ensure that resolutions were matched across the wavelength range of the datasets. The best results were obtained using 12 iterations. The deconvolution was carried out using the Python scikit-image restoration tools. Post-deconvolution, we confirmed flux conservation by comparing the flux of lines analysed in this work before and after deconvolution. We also verified that no artefacts were introduced by inspecting continuum-subtracted line maps (see ‘Continuum-subtracted line maps’ for their generation) and confirmed that the emission features sharpened to the same resolution level, with PSF broadening as a function of wavelength effectively removed.

The deconvolution model PSF was derived using the JWST WebbPSF software package⁵¹ and commissioning observations of a point source. Although WebbPSF can generate representative model PSFs for NIRSpec with time-specific optical path differential files (OPD), these models do not include the full optical path of the IFU, such as the grating distortions and IFU slicing optics. To incorporate the IFU optical path, we devised a new methodology (Beck et al. in preparation) that relies on convolving the WebbPSF models with a kernel generated from the commissioning data of a point source observed in IFU mode (Programme ID 1128). In doing this, the kernel data cube takes into account optical differences between the empirical point source data and the PSF model calculations. This kernel can, hence, be used with the appropriate WebbPSF OPD calculation at the time of an observation to create a noise-free PSF matched to any science data. The deconvolution PSF model used for this study was constructed by using the WebbPSF OPD model for the time of the observations of HH 30 (26 September 2022; with a NIRSpec wavefront error of $75\ \text{nm r.m.s.}$) and convolving by our kernel to match the science data presented here.

Continuum-subtracted line maps

First, we generated total spectra summing up the flux over the entire NIRSpec IFU. These spectra are shown in Fig. 1. In addition to some of the strongest features and emission lines of interest, we also mark the NIRSpec detector gaps with semitransparent colours. Note that by plotting the minimum and maximum wavelength cutoffs of the IFU slices, we have taken the most conservative approach. The wavelength range over which flux is lost depends on the set of slices where the source flux extends. Hence, some flux is recovered in the semitransparent regions, especially for compact sources like FS Tau B.

To create line-only maps for the [Fe II] and H_2 lines, we adopted the method outlined by ref. 52. First, we used the total spectra and `scipy.optimize.curve_fit` to fit a Gaussian profile on top of the continuum and to determine the total flux (reported in Table 2) and the average line centroid and full-width at half-maximum (FWHM). Monte Carlo simulations showed that the uncertainty of the line flux due to the standard deviation in the nearby continuum was at most a few percent, lower than the 10% absolute flux calibration uncertainty of NIRSpec²⁰. Next, we extracted the flux at each spaxel and fitted a Gaussian plus continuum. We considered a line to be detected if the peak value of the Gaussian profile was at least three times the standard deviation of the continuum and if the standard deviation around the fitted line decreased after subtracting the best-fitting Gaussian plus continuum. When a line was detected, we calculated the area of the Gaussian for the line-only map and stored the centroid to determine which portion of the jet or wind was blueshifted. When no line was detected, we refitted only the continuum and set a 1σ upper limit for the line-only map using the standard deviation of the continuum-subtracted data and the average FWHM. The continuum-only map was derived by averaging the continuum across the line centroid \pm FWHM. Although not shown here, we also generated line-only maps for the H_2 $2.12\ \mu\text{m}$ and $5.05\ \mu\text{m}$ transitions with integrated fluxes (Supplementary Table 1). Their morphologies were the same as that of the H_2 $0 \rightarrow 0\text{S}(9)$ line, which we focus on here because it suffered less than the $2.12\ \mu\text{m}$ line from scattering close to the disk plane and it is brighter than the $5.05\ \mu\text{m}$ line.

To construct the continuum-subtracted CO ($v = 1 \rightarrow 0$) map, we expanded the method above by fitting, at each spaxel, several Gaussian profiles across various wavelength segments, all sharing a common continuum. We used the ^{12}CO and ^{13}CO line list from the HITRAN database⁵³, supplemented by other lines within the CO ($v = 1 \rightarrow 0$) fundamental band (<https://pdrs4all.org/seps/#highly-processed-data-products>). The line-only map was generated by summing the areas of all detected ^{12}CO lines. In spaxels where lines were not detected, we provided a 3σ upper limit, calculated using the standard deviation of the data after continuum subtraction and the average ^{12}CO FWHM from fitting lines in the total NIRSpec IFU spectrum.

Jet and wind morphologies

To measure the jet PA, we used the continuum-subtracted [Fe II] $1.644\ \mu\text{m}$ map generated with the default rotation in the pipeline script provided by the Space Telescope Science Institute so that north was pointing up along the y axis. For each pixel along the x axis, we extracted the corresponding y array, smoothed it and found its peak value (y_{peak}). We then performed a linear fit of the x values and the identified y_{peak} s using the `sklearn.RANSACRegressor`. The jet PA is the angle between this best-fitting line and the direction of north. We repeated the extraction, peak identification and linear fit across different sets of (x, y) points that exhibit jet emission. Next, we analysed the distribution of the jet PAs and computed the mode, the most frequently occurring PA, and the standard deviation. These are the values reported in Table 2. Note that in all cases, the jet PA is found to be perpendicular to the disk PA within the quoted uncertainties.

We determined the blueshifted side of the jet from the Gaussian line centroid map, which was constructed as discussed in ‘Continuum-subtracted line maps’. We then rotated all line-only and

continuum maps to an angle that aligned the blueshifted component of the jet with the upper part of the y axis on the panel. The jet's emission pinpoints the star's position along the x axis. However, locating the star on the y axis was more challenging due to the systems being observed close to edge-on. This orientation results in the circumstellar disk obscuring partially or completely the star's emission. For HH 30, IRAS 04302 and Tau 042021, whose disks are inclined by more than 80° , the continuum map traces the flared disk surface, with no emission near the disk plane. For these cases, we extracted a profile along the jet emission and identified the midpoint of the non-emissive, or 'dark', continuum valley. This midpoint was assigned as the star's y axis location as well as the disk plane. For FS Tau B, with the disk inclined at $\sim 70^\circ$, the continuum emission appeared point-like (Fig. 2) and probably traces scattered light in proximity to the central star. We assigned the star's y axis position to the pixel just below the peak of the continuum emission.

We used the gradual broadening of the jet emission away from the disk plane to estimate the jet semi-opening angles (θ_j) reported in Table 2. First, we performed horizontal cuts across the [Fe II] rotated line-only images, fitted a Gaussian profile and measured its FWHM. Next, we assessed potential artificial broadening of the jet's FWHM due to scattering near the disk plane, along with any insufficient FWHM sampling. For FS Tau B, IRAS 04302 and Tau 042021, note that the peak of the jet emission spreads over two columns. Consequently, any FWHM measurement below 1.7 pixels (equivalent to $0.17''$) was considered to be undersampled. This is evidenced by the near-constant jet FWHM for FS Tau B and Tau 042021 at distances below $0.5''$ from the disk plane, as shown in Fig. 3. Hence, we excluded any data points with $\text{FWHM} < 0.17''$ when determining the jets' semi-opening angles. In contrast, the peak jet emission in HH 30 was more narrowly confined along a single column, which mitigated the sampling issue. For this source, we further compared our FWHM versus distance with that obtained from higher-resolution spectral images of the [S II] $6,731 \text{ \AA}$ and [O I] $6,300 \text{ \AA}$ lines recorded by the space telescope imaging spectrograph onboard the Hubble Space Telescope³⁷ and determined that the [Fe II] jet becomes resolvable at distances greater than $1''$ from the disk plane. Only these resolvable points were used in our analysis. Ordinary least squares fitting was then applied to the data points unaffected by scattering or poor sampling, which are represented by filled circles in Fig. 3. The jet semi-opening angle (θ_j) was calculated from the slope of the best-fitting relation. This value along with its 1σ uncertainty derived from the covariance matrix are provided in Table 2. For FS Tau B and HH 30, for which jet semi-opening angles have previously been reported in the literature^{37,54}, our values align with the published ones within the estimated uncertainties.

The wind semi-opening angles (θ_w) and geometric radii (R_{geo}) reported in Table 2 were measured for the rotated $\text{H}_2 \text{ } 0 \rightarrow 0 \text{ S}(9)$ line-only image. To trace the wind's outer contours, we developed two approaches. The first one follows ref. 55 and relies on calculating the second-order derivative of horizontal cuts across the wind emission and finding its zero values. These values indicate the inflection points that define the wind's edge. However, for complex patchy emission, like that from IRAS 04302, the method finds too many inflection points that need to be handled manually. As such, we developed a more robust approach that relies on fitting Gaussian profiles, typically two but see below, to the same horizontal cuts. We verified for HH 30 that the wind's edges from the first method are equivalent to the Gaussian centroids plus or minus half of its FWHM, depending on the wind's location with respect to the central axis. For FS Tau B and HH 30, one Gaussian $\pm 0.5 \times \text{FWHM}$ was used when approaching the disk plane. The Gaussian fitting method was applied to all sources and used to determine the wind's properties. Supplementary Fig. 1 demonstrates this technique for HH 30. To evaluate if the wind's shape exhibits symmetry around the central axis, we analysed the edges on either side separately. We fitted the edges versus the distance from the star using ordinary least squares. The semi-opening angles (θ_w) of the wind were then calculated

as the angles between the best-fitting lines and the vertical y axis. The geometric radii (R_{geo}) were determined by the intersection points of these best-fitting lines with the disk's plane, marked by the star's location on the y axis. Further, 1σ uncertainties for θ_w and R_{geo} were calculated and are reported in Table 2 and for the CO ($v = 1 \rightarrow 0$) in HH 30 in the caption of Fig. 4.

Data availability

The JWST data used in this paper can be found at the Mikulski Archive for Space Telescope under programme IDs 1621 (ref. 56) and 1128 (ref. 57). The first programme covers the four edge-on disks, and the second has the commissioning data used to generate the NIRSpect PSF. Both raw data and fully processed pipeline data can be downloaded from the archive. The spectra integrated over the NIRSpect IFU (Fig. 1) as well as the line-only and continuum maps (Fig. 2) are available via Figshare at <https://doi.org/10.6084/m9.figshare.26387977> (ref. 58).

Code availability

The data were reduced with the JWST calibration pipeline v.1.13.4.dev19+gbddb39c6. Upon request, the first author (I.P.) will provide the Python scripts used to analyse the data and generate the figures.

References

- Balbus, S. A. & Hawley, J. F. A powerful local shear instability in weakly magnetized disks. I. Linear analysis. *Astrophys. J.* **376**, 214 (1991).
- Lesur, G. et al. in *Protostars and Planets VII* (eds Inutsuka, S. et al.) 465–500 (ASP, 2023).
- Suzuki, T. K., Ogiwara, M., Morbidelli, A., Crida, A. & Guillot, T. Evolution of protoplanetary discs with magnetically driven disc winds. *Astron. Astrophys.* **596**, A74 (2016).
- Taki, T., Kuwabara, K., Kobayashi, H. & Suzuki, T. K. New growth mechanism of dust grains in protoplanetary disks with magnetically driven disk winds. *Astrophys. J.* **909**, 75 (2021).
- Kimmig, C. N., Dullemond, C. P. & Kley, W. Effect of wind-driven accretion on planetary migration. *Astron. Astrophys.* **633**, A4 (2020).
- Wang, L., Bai, X.-N. & Goodman, J. Global simulations of protoplanetary disk outflows with coupled non-ideal magnetohydrodynamics and consistent thermochemistry. *Astrophys. J.* **874**, 90 (2019).
- Shu, F. et al. Magnetocentrally driven flows from young stars and disks. I. A generalized model. *Astrophys. J.* **429**, 781 (1994).
- Alexander, R., Pascucci, I., Andrews, S., Armitage, P. & Cieza, L. in *Protostars and Planets VI* (eds Beuther, H. et al.) 475–496 (ASP, 2014).
- Panoglou, D. et al. Molecule survival in magnetized protostellar disk winds. I. Chemical model and first results. *Astron. Astrophys.* **538**, A2 (2012).
- Shu, F. H., Najita, J., Ostriker, E. C. & Shang, H. Magnetocentrally driven flows from young stars and disks. V. Asymptotic collimation into jets. *Astrophys. J. Lett.* **455**, L155 (1995).
- Matsuyama, I., Johnstone, D. & Hollenbach, D. Dispersal of protoplanetary disks by central wind stripping. *Astrophys. J.* **700**, 10–19 (2009).
- Cunningham, A., Frank, A. & Hartmann, L. Wide-angle wind-driven bipolar outflows: high-resolution models with application to source I of the Becklin-Neugebauer/Kleinmann-low OMC-I region. *Astrophys. J.* **631**, 1010–1021 (2005).
- Wang, L. & Goodman, J. Hydrodynamic photoevaporation of protoplanetary disks with consistent thermochemistry. *Astrophys. J.* **847**, 11 (2017).

14. Evans II, N. J. et al. The Spitzer c2d legacy results: star-formation rates and efficiencies; evolution and lifetimes. *Astrophys. J. Suppl. Ser.* **181**, 321–350 (2009).
15. Gangi, M. et al. GIARPS high-resolution observations of T Tauri stars (GHOsT). II. Connecting atomic and molecular winds in protoplanetary disks. *Astron. Astrophys.* **643**, A32 (2020).
16. Pascucci, I. et al. in *Protostars and Planets VII* (eds Inutsuka, S. et al.) 567 (ASP, 2023).
17. Agra-Amboage, V. et al. Origin of the wide-angle hot H₂ in DG Tauri. New insight from SINFONI spectro-imaging. *Astron. Astrophys.* **564**, A11 (2014).
18. Beck, T. L. & Bary, J. S. A search for spatially resolved infrared rovibrational molecular hydrogen emission from the disks of young stars. *Astrophys. J.* **884**, 159 (2019).
19. Arulanantham, N. et al. JWST MIRI MRS images of disk winds, water, and CO in an edge-on protoplanetary disk. *Astrophys. J. Lett.* **965**, L13 (2024).
20. Böker, T. et al. In-orbit performance of the near-infrared spectrograph NIRSpec on the James Webb Space Telescope. *Publ. Astron. Soc. Pac.* **135**, 038001 (2023).
21. Villenave, M. et al. Observations of edge-on protoplanetary disks with ALMA. I. Results from continuum data. *Astron. Astrophys.* **642**, A164 (2020).
22. Luhman, K. L. The stellar membership of the Taurus star-forming region. *Astron. J.* **156**, 271 (2018).
23. Furlan, E. et al. The Spitzer infrared spectrograph survey of T Tauri stars in Taurus. *Astrophys. J. Suppl. Ser.* **195**, 3 (2011).
24. Crapsi, A., van Dishoeck, E. F., Hogerheijde, M. R., Pontoppidan, K. M. & Dullemond, C. P. Characterizing the nature of embedded young stellar objects through silicate, ice and millimeter observations. *Astron. Astrophys.* **486**, 245–254 (2008).
25. Di Francesco, J., Johnstone, D., Kirk, H., MacKenzie, T. & Ledwosinska, E. The SCUBA legacy catalogues: submillimeter-continuum objects detected by SCUBA. *Astrophys. J. Suppl. Ser.* **175**, 277–295 (2008).
26. Reipurth, B., Chini, R., Kreysa, E. & Sievers, A. Cold dust around Herbig-Haro energy sources – a 1300-micron survey. *Astron. Astrophys.* **273**, 221–238 (1993).
27. Andrews, S. M. & Williams, J. P. Circumstellar dust disks in Taurus-Auriga: the submillimeter perspective. *Astrophys. J.* **631**, 1134–1160 (2005).
28. Andrews, S. M., Rosenfeld, K. A., Kraus, A. L. & Wilner, D. J. The mass dependence between protoplanetary disks and their stellar hosts. *Astrophys. J.* **771**, 129 (2013).
29. Takami, M. et al. Subaru IR echelle spectroscopy of Herbig-Haro driving sources. I. H₂ and [Fe II] emission. *Astrophys. J.* **641**, 357–372 (2006).
30. Bacciotti, F., Eisloffel, J. & Ray, T. P. The physical properties of the HH 30 jet from HST and ground-based data. *Astron. Astrophys.* **350**, 917–927 (1999).
31. Nisini, B. et al. Connection between jets, winds and accretion in T Tauri stars. The X-shooter view. *Astron. Astrophys.* **609**, A87 (2018).
32. White, R. J. & Hillenbrand, L. A. On the evolutionary status of class I stars and Herbig-Haro energy sources in Taurus-Auriga. *Astrophys. J.* **616**, 998–1032 (2004).
33. Davis, C. J. et al. VLT integral field spectroscopy of embedded protostars: using near-infrared emission lines as tracers of accretion and outflow. *Astron. Astrophys.* **528**, A3 (2011).
34. Nisini, B. et al. PROJECT-J: JWST observations of HH46 IRS and its outflow. Overview and first results. *Astrophys. J.* **967**, 168 (2024).
35. Jensen, S. K. et al. Spectroastrometric survey of protoplanetary disks with inner dust cavities. *Astron. J.* **167**, 115 (2024).
36. Eisloffel, J. & Mundt, R. Imaging and kinematic studies of young stellar object jets in Taurus. *Astron. J.* **115**, 1554–1575 (1998).
37. Hartigan, P. & Morse, J. Collimation, proper motions, and physical conditions in the HH 30 jet from Hubble Space Telescope slitless spectroscopy. *Astrophys. J.* **660**, 426–440 (2007).
38. Louvet, F. et al. The HH30 edge-on T Tauri star. A rotating and precessing monopolar outflow scrutinized by ALMA. *Astron. Astrophys.* **618**, A120 (2018).
39. Erkal, J. et al. Launching the asymmetric bipolar jet of DO Tau. *Astron. Astrophys.* **650**, A46 (2021).
40. Blandford, R. D. & Payne, D. G. Hydromagnetic flows from accretion disks and the production of radio jets. *Mon. Not. R. Astron. Soc.* **199**, 883–903 (1982).
41. Ai, T.-H., Liu, C.-F., Shang, H., Johnstone, D. & Krasnopolsky, R. A unified model for bipolar outflows from young stars: kinematic and mixing structures in HH 30. *Astrophys. J.* **964**, 147 (2024).
42. Rabenahary, M., Cabrit, S., Meliani, Z. & Pineau des Forêts, G. Wide-angle protostellar outflows driven by narrow jets in stratified cores. *Astron. Astrophys.* **664**, A118 (2022).
43. Liang, L., Johnstone, D., Cabrit, S. & Kristensen, L. E. Steady wind-blown cavities within infalling rotating envelopes: application to the broad velocity component in young protostars. *Astrophys. J.* **900**, 15 (2020).
44. Komaki, A., Nakatani, R. & Yoshida, N. Radiation hydrodynamics simulations of protoplanetary disks: stellar mass dependence of the disk photoevaporation rate. *Astrophys. J.* **910**, 51 (2021).
45. Rab, C. et al. Interpreting molecular hydrogen and atomic oxygen line emission of T Tauri disks with photoevaporative disk-wind models. *Astron. Astrophys.* **668**, A154 (2022).
46. Béthune, W., Lesur, G. & Ferreira, J. Global simulations of protoplanetary disks with net magnetic flux. I. Non-ideal MHD case. *Astron. Astrophys.* **600**, A75 (2017).
47. Giacalone, S., Teitler, S., Königl, A., Krijt, S. & Ciesla, F. J. Dust transport and processing in centrifugally driven protoplanetary disk winds. *Astrophys. J.* **882**, 33 (2019).
48. Bushouse, H. et al. *JWST Calibration Pipeline* (STScI, 2023).
49. Richardson, W. H. Bayesian-based iterative method of image restoration. *J. Opt. Soc. Am.* **62**, 55 (1972).
50. Lucy, L. B. An iterative technique for the rectification of observed distributions. *Astron. J.* **79**, 745 (1974).
51. Perrin, M. D. et al. Updated point spread function simulations for JWST with WebbPSF. In *Proc. SPIE Conference Series, Space Telescopes and Instrumentation 2014: Optical, Infrared, and Millimeter Wave* Vol. 9143 (eds Oschmann, J. M. Jr et al.) 91433X (SPIE, 2014).
52. Beck, T. L., McGregor, P. J., Takami, M. & Pyo, T.-S. Spatially resolved molecular hydrogen emission in the inner 200 au environments of classical T Tauri stars. *Astrophys. J.* **676**, 472–489 (2008).
53. Gordon, I. E. et al. The HITRAN2020 molecular spectroscopic database. *J. Quant. Spectrosc. Radiat. Transf.* **277**, 107949 (2022).
54. Mundt, R., Ray, T. P. & Raga, A. C. Collimation of stellar objects – constraints from the observed spatial structure. II. Observational results. *Astron. Astrophys.* **252**, 740–761 (1991).
55. Habel, N. M. et al. An HST survey of protostellar outflow cavities: does feedback clear envelopes? *Astrophys. J.* **911**, 153 (2021).
56. Pascucci, I. Data from paper ‘The nested morphology of disk winds from young stars revealed by JWST/NIRSpec observations’. *Mikulski Archive for Space Telescopes* <https://doi.org/10.17909/3z83-wx27> (2024).
57. Pascucci, I. Commissioning data used in ‘The nested morphology of disk winds from young stars revealed by JWST/NIRSpec observations’. *Mikulski Archive for Space Telescopes* <https://doi.org/10.17909/325d-tm53> (2024).
58. Pascucci, I. et al. The nested morphology of disk winds from young stars revealed by JWST/NIRSpec observations. *Figshare* <https://doi.org/10.6084/m9.figshare.26387977> (2024).

59. Simon, M. et al. Masses and implications for ages of low-mass pre-main-sequence stars in Taurus and Ophiuchus. *Astrophys. J.* **884**, 42 (2019).
60. Duchêne, G. et al. JWST imaging of edge-on protoplanetary disks. I. Fully vertically mixed 10 μm grains in the outer regions of a 1000 au disk. *Astron. J.* **167**, 77 (2024).

Acknowledgements

This work is based on observations made with the NASA/ESA/CSA JWST. The data were obtained from the Mikulski Archive for Space Telescopes at the Space Telescope Science Institute, which is operated by the Association of Universities for Research in Astronomy, Inc., under NASA contract NAS 5-03127 for JWST. These observations are associated with the general observer cycle 1 programme 1621 (PI I. Pascucci). I.P. and N.S.B. acknowledge partial support from NASA and the Space Telescope Science Institute (GO Grant No. JWST-GO-01621.001, PI I.P.). S.C. acknowledges funding from the funding from the Scientific Council of Observatoire de Paris and the national programme Physique et Chimie du Milieu Interstellaire of Centre National de la Recherche Scientifique, a programme operated through the Institut National des Sciences de l'Univers with Institut National de Chimie and Institut National de Physique and co-funded by the Commissariat à l'Energie Atomique et aux Energies Alternatives and Centre National d'Etudes Spatiales. K.S. and D.S. acknowledge support from the European Research Council (ERC) under the Horizon 2020 Framework Program through ERC Advanced Grant Origins 83 24 28, PI Th. Henning. G.D. acknowledges support from the ERC under the European Union's Horizon Europe research and innovation programme (Grant Agreement No. 101053020, Project Dust2Planets, PI F. Ménard). M.V. acknowledges support from the ERC under the European Union's Horizon Europe Research & Innovation Programme (Grant Agreement No. 101039651, DiscEvol, PI G. Rosotti). I.P. thanks D. Deng and F. Long for an initial exploration of the ALMA data for our sources. We acknowledge the use of the following packages: api, Astropy, NumPy, SciPy, sklearn, Matplotlib and pandas.

Author contributions

I.P. led the proposal, carried out the analysis and wrote the paper. T.B., S.C., S.E., J.N., U.G., C.S., S.B., S.K., J.M., M.R., K.S. and D.S.

contributed to the planning and writing of the JWST proposal. N.S.B. used the JWST pipeline to perform the data reduction. T.B. assisted in planning the observations, in the data reduction and in the PSF deconvolution of the reduced data cubes. F.L. provided the ALMA CO (2 \rightarrow 1) data for HH 30. B.S. contributed to the initial script used to generate the CO ($v=1\rightarrow 0$) map and the RGB figures. S.C., S.E., J.N. and U.G. made substantial contributions to the interpretation of the results. All authors participated in the discussion of the results or commented on the paper.

Competing interests

The authors declare no competing interests.

Additional information

Supplementary information The online version contains supplementary material available at <https://doi.org/10.1038/s41550-024-02385-7>.

Correspondence and requests for materials should be addressed to Ilaria Pascucci.

Peer review information *Nature Astronomy* thanks Manuele Gangi and the other, anonymous, reviewer(s) for their contribution to the peer review of this work.

Reprints and permissions information is available at www.nature.com/reprints.

Publisher's note Springer Nature remains neutral with regard to jurisdictional claims in published maps and institutional affiliations.

Springer Nature or its licensor (e.g. a society or other partner) holds exclusive rights to this article under a publishing agreement with the author(s) or other rightsholder(s); author self-archiving of the accepted manuscript version of this article is solely governed by the terms of such publishing agreement and applicable law.

© The Author(s), under exclusive licence to Springer Nature Limited 2024